

High-Resolution Low-Field Molecular Magnetic Resonance Imaging of Hyperpolarized Liquids

Aaron M. Coffey,^{†,‡} Kirill V. Kovtunov,^{§,||} Danila A. Barskiy,^{§,||} Igor V. Koptug,^{§,||} Roman V. Shchepin,[†] Kevin W. Waddell,^{†,⊥} Ping He,[#] Kirsten A. Groome,[#] Quinn A. Best,[#] Fan Shi,[#] Boyd M. Goodson,[#] and Eduard Y. Chekmenev^{*,†,‡,⊗,○}

[†]Vanderbilt University Institute of Imaging Science (VUIIS) and Department of Radiology, Vanderbilt University, Nashville, Tennessee 37232, United States

[‡]Department of Biomedical Engineering, Vanderbilt University, Nashville, Tennessee 37235, United States

[§]International Tomography Center, 3A Institut'skaya St., Novosibirsk 630090, Russia

^{||}Novosibirsk State University, 2 Pirogova St., Novosibirsk, 630090, Russia

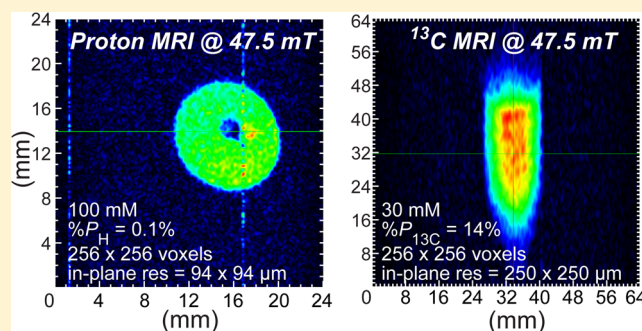
[⊥]Department of Physics and Astronomy, Vanderbilt University, Nashville, Tennessee 37232, United States

[#]Department of Chemistry & Biochemistry, Southern Illinois University, Carbondale, Illinois 62901, United States

[⊗]Department of Biochemistry and [○]Vanderbilt-Ingram Cancer Center, Vanderbilt University, Nashville, Tennessee 37232, United States

S Supporting Information

ABSTRACT: We demonstrate the feasibility of microscale molecular imaging using hyperpolarized proton and carbon-13 MRI contrast media and low-field (47.5 mT) preclinical scale (38 mm i.d.) 2D magnetic resonance imaging (MRI). Hyperpolarized proton images with $94 \times 94 \mu\text{m}^2$ spatial resolution and hyperpolarized carbon-13 images with $250 \times 250 \mu\text{m}^2$ in-plane spatial resolution were recorded in 4–8 s (largely limited by the electronics response), surpassing the in-plane spatial resolution (i.e., pixel size) achievable with micro-positron emission tomography (PET). These hyperpolarized proton and ^{13}C images were recorded using large imaging matrices of up to 256×256 pixels and relatively large fields of view of up to $6.4 \times 6.4 \text{ cm}^2$. ^{13}C images were recorded using hyperpolarized 1- ^{13}C -succinate- d_2 (30 mM in water, $\%P_{^{13}\text{C}} = 25.8 \pm 5.1\%$ (when produced) and $\%P_{^{13}\text{C}} = 14.2 \pm 0.7\%$ (when imaged), $T_1 = 74 \pm 3 \text{ s}$), and proton images were recorded using ^1H hyperpolarized pyridine (100 mM in methanol- d_4 , $\%P_{^1\text{H}} = 0.1 \pm 0.02\%$ (when imaged), $T_1 = 11 \pm 0.1 \text{ s}$). Both contrast agents were hyperpolarized using parahydrogen (>90% para-fraction) in an automated 5.75 mT parahydrogen induced polarization (PHIP) hyperpolarizer. A magnetized path was demonstrated for successful transportation of a ^{13}C hyperpolarized contrast agent (1- ^{13}C -succinate- d_2 , sensitive to fast depolarization when at the Earth's magnetic field) from the PHIP polarizer to the 47.5 mT low-field MRI. While future polarizing and low-field MRI hardware and imaging sequence developments can further improve the low-field detection sensitivity, the current results demonstrate that microscale molecular imaging *in vivo* is already feasible at low (<50 mT) fields and potentially at low ($\sim 1 \text{ mM}$) metabolite concentrations.



Molecular imaging¹ differs from traditional medical imaging modalities by utilizing probes known as biomarkers to image particular biochemical targets or metabolic pathways. These molecular imaging probes typically require use of radioactive nuclei, e.g., ^{18}F -fluorodeoxyglucose for positron emission tomography (PET),² or chemical modification of the tracer molecules, e.g., fluorescent contrast media.³ In comparison, hyperpolarized magnetic resonance imaging (HP MRI) contrast media are uniquely free from the above shortcomings because nonradioactive nuclei such as ^{13}C in naturally occurring metabolites are being traced. Moreover, the signatures of injected HP MRI contrast agents and their

metabolites can be spectrally differentiated to yield additional molecular information,⁴ an advantage that has already been exploited in clinical trials for prostate cancer.⁵ Hyperpolarization^{4,6,7} is a key step in the preparation of these agents; generally, conventional magnetic resonance (MR) methods are otherwise not sensitive enough to track and image such molecules *in vivo* because of low concentrations and as a consequence of the miniscule equilibrium nuclear spin

Received: May 4, 2014

Accepted: August 19, 2014

Published: August 27, 2014

polarization ($P \leq 10^{-5}$). Although fundamentally transient in nature, HP spin states can be prepared by increasing the nuclear spin polarization to nearly 100% in some cases, directly translating to orders-of-magnitude enhancement of MR sensitivity. To date, near-unity levels of polarization have been achieved for several nuclei. For example, spin exchange optical pumping (SEOP) has produced $P_{129\text{Xe}}$ values as high as ~ 0.9 for Xe gas.⁸ Similarly, values as high as $P_{\text{H}} = 0.9$ for protons and $P_{13\text{C}} = 0.7$ for carbon⁹ have been achieved by dissolution dynamic nuclear polarization (DNP). Alternatively, the chemically based hyperpolarization techniques such as parahydrogen induced polarization (PHIP)¹⁰ and signal amplification by reversible exchange (SABRE)¹¹ utilize the pure spin order of the singlet state of protons in parahydrogen as the polarization source.¹²

When slowly relaxing nuclear spins with spin–lattice relaxation time (T_1) of tens of seconds are hyperpolarized in biologically relevant molecules (e.g., ^{13}C -pyruvate), they can be successfully used to image cellular metabolism in living organisms^{4,5} to act as HP contrast agents (HCAs) enabling true molecular imaging.¹³ HP agents have already served as useful probes for reporting on metabolic changes in several deadly diseases¹⁴ including cancer,¹⁵ where the agents fulfill the role of imaging biomarkers.⁴ Moreover, these agents can noninvasively report on early response to treatment¹⁶ and enable disease grading.¹⁷

While HCA technology provides clear benefits of rich molecular information content, this emerging advanced imaging modality engenders additional complexity and costs. Normally a relatively expensive “hyperpolarizer” for on-site HCA production¹⁸ is required, which must be situated in close proximity to a high-field MRI scanner equipped with multinuclear capability. For example, the leading HCA technology, dissolution-DNP, is being tested on a 3 T MRI platform.⁵ Combined with the relatively low throughput rate of patient examination of high-field MRI (≥ 1.5 T), HCA technology in its present state is likely to carry a high molecular imaging examination cost similar to that of PET imaging. In addition to the expected financial burden to first-world economies, such a trend would likely render this technology unavailable to patient populations in poorer countries comprising most of the world’s population.

However, HCA technology offers one more significant technological advantage that has largely remained untapped: the induced nuclear spin hyperpolarization is independent of the MRI scanner’s magnetic field. We have recently provided a theoretical basis with experimental evidence that low-field MRI can be more sensitive than high-field MRI for HP detection. This was achieved through the introduction of resonance frequency-optimized MRI radio-frequency (rf) coils that mitigate unfavorable scaling of sensitivity with frequency.¹⁹ Low-field MRI (≤ 0.05 T) enjoys several advantages over high field. It is significantly less expensive due to reduced magnet costs. It is also a significantly higher examination throughput technique, because no time for patient-tailored scanner preparation (i.e., B_0 and B_1 field shimming) is needed. Furthermore, it has also been recently shown that patient rf power deposition is negligible at such low operating frequencies²⁰ making it a significantly safer imaging modality.

Here, the feasibility of low-field molecular imaging with a very high spatial resolution ($94 \times 94 \mu\text{m}^2$) is demonstrated at 47.5 mT for ^1H and ^{13}C detection of HCA with ^1H HP pyridine and ^{13}C HP 1- ^{13}C -succinate- d_2 . The HCAs were

prepared using the parahydrogen-based hyperpolarization techniques of SABRE and PHIP, respectively. These techniques are not instrumentation-demanding and offer high-throughput production of HP contrast media and thus have the potential to enable low-cost production of HCAs for clinical imaging. When combined with low-field MRI, such HCA production methods should ultimately enable a high-throughput molecular-imaging platform for clinical use at a relatively low cost.

RESULTS

Hyperpolarization of Contrast Agents in PHIP Polarizer. Pyridine (Py) protons were hyperpolarized to $\%P_{\text{H}} = 0.1 \pm 0.02\%$ (average polarization per each proton (five in total) corresponding to an enhancement factor $\epsilon \approx 5000$ at 47.5 mT), which was confirmed spectroscopically at 47.5 mT using a reference NMR signal from thermally polarized water in accordance with the referencing scheme previously reported.^{8,21} Using the experimentally determined T_1 of 11.1 ± 0.1 s at 47.5 mT (average T_1 for all HP protons of Py) and an estimated 12 s delivery time from the PHIP polarizer to the low-field MRI scanner, it was concluded that the initial Py hyperpolarization achieved at 5.75 mT was $\sim 0.3 \pm 0.06\%$ (per each proton). 1- ^{13}C -Succinate- d_2 was hyperpolarized to $\%P_{13\text{C}} = 25.8 \pm 5.1\%$ (30 mM substrate injected into 7 atm of para- H_2 during 5 s reaction time at 73 °C) as measured *in situ* by the 5.75 mT PHIP polarizer using a 30° excitation rf pulse. This *in situ* ^{13}C detection allowed for quality assurance of the HCA prior to delivery to the low-field MRI system. The 30° rf pulse consumed $\sim 13\%$ of the ^{13}C magnetization while leaving the remaining 87% (i.e., $\%P_{13\text{C}} = 22.4 \pm 4.4\%$) available for further use.

“HyperBridge” and “HyperGate” Use for Hyperpolarized ^{13}C -Succinate- d_2 . While transfer of HP agents has been recently demonstrated^{22,23} using a magnetic pathway, such work was conducted at 0.8 T using a significantly more sophisticated rigid structure. In this work, a two-piece magnetic pathway with mT fields was developed. The first device used here, dubbed the “HyperBridge”, consisted of a series of one-sided flexible magnetized strips (~ 0.5 in. wide, Figure 1) assembled into a single flexible line. The $1/8$ in. o.d. ($1/16$ in. i.d.) tubing attached to this flexible line is used for transferring the HP solution while a static magnetic field of ~ 14 –50 mT is maintained. A second device, dubbed the “HyperGate”, was used to generate a 4–6 mT magnetic field over ~ 1 ft³ at the entrance of the low-field MRI magnet. While some HCAs such as HP 2-hydroxyethyl 1- ^{13}C -propionate (HEP) can be exposed to nearly zero magnetic field without substantial loss of polarization, other HCAs clearly require hyperpolarization protection by a sufficient static magnetic field during the transfer from hyperpolarizer to the MRI scanner.^{22,23} Thus, the HyperBridge and HyperGate were not used with HP Py but were required for HP 1- ^{13}C -succinate- d_2 .

The combined efficacy of the HyperBridge and HyperGate was tested by ^{13}C hyperpolarization detection before and after HCA transfer between the PHIP polarizer and the MRI scanner. The ^{13}C T_1 of 1- ^{13}C -succinate- d_2 in aqueous solution was 74 ± 3 s and 75 ± 3 s at 5.75 mT and 47.5 mT, respectively. Although the HCA passes through variable magnetic fields in the range of ~ 4 –50 mT, a single value of $T_1 = 75$ s was used to estimate T_1 hyperpolarization losses based on the above results at 5.75 mT and 47.5 mT. In one experiment, $\%P_{13\text{C}} = 25.8 \pm 5.1\%$ was produced in the PHIP polarizer. This sample was delivered via HyperBridge and

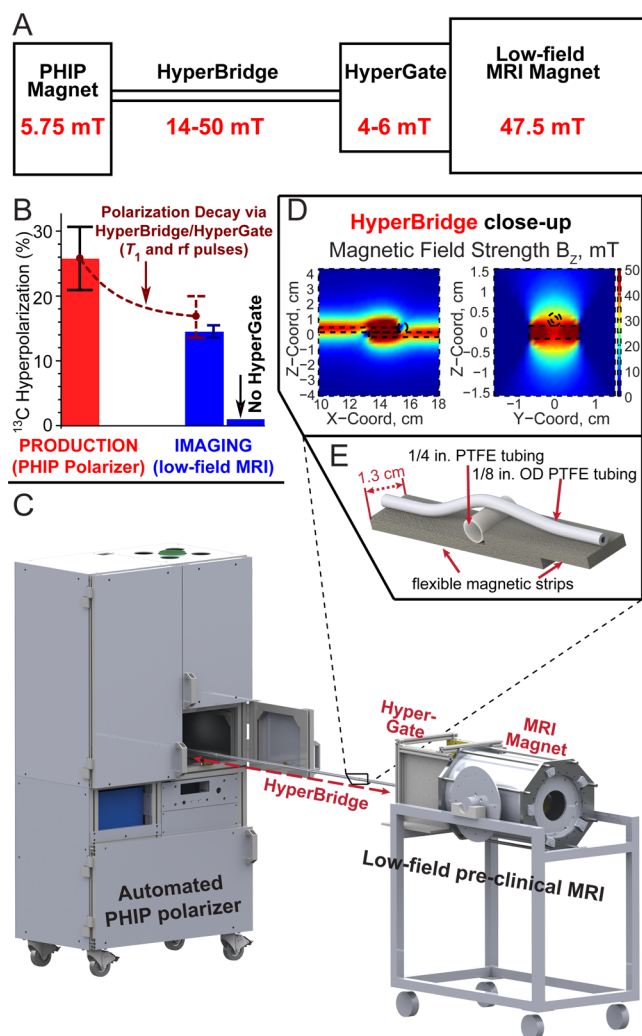


Figure 1. (A) Diagram of the experimental setup interfacing an automated parahydrogen induced polarization (PHIP) hyperpolarizer operating at 5.75 mT with a low-field (47.5 mT) preclinical MRI scanner (NMR console not shown) by using the HyperBridge and HyperGate to maintain the PHIP hyperpolarization of $1\text{-}^{13}\text{C}$ -succinate- d_2 during transfer. The inset shows additional details of the HyperBridge; the HyperBridge and HyperGate are fully described in Figures S1–S3 in the Supporting Information. (B) Hyperpolarization chart demonstrating the efficacy of transportation of hyperpolarized $1\text{-}^{13}\text{C}$ -succinate- d_2 . ^{13}C hyperpolarization was measured *in situ* of the PHIP polarizer (with a 30° rf pulse) before the transfer and in the MRI scanner (with a 15° rf pulse) after the transfer. (C) 3D-rendering of the experimental setup. (D, E) Close-up of the HyperBridge.

HyperGate into the MRI scanner over a 22 ± 2 s period, wherein the total losses (from T_1 decay and application of the sampling rf pulse in the PHIP polarizer) should diminish the ^{13}C hyperpolarization by a factor of 1.54 to yield an estimated $\%P_{^{13}\text{C}}$ value of $16.7 \pm 3.3\%$ (in the MRI scanner), Figure 1A. Indeed, $\%P_{^{13}\text{C}} = 14.2 \pm 0.7\%$ was measured experimentally, corresponding to an enhancement factor $\epsilon \approx 3\,500\,000$ at 47.5 mT, which indicated that primary losses were largely due to T_1 relaxation and rf excitation. A control experiment performed with a similar ^{13}C hyperpolarization level but without the HyperGate yielded a ^{13}C hyperpolarization of $<1\%$ at 47.5 mT (Figure 1B), demonstrating a significant loss of hyperpolarization and the efficacy of the HyperBridge and HyperGate.

2D Low-Field MRI of HCAs. HP proton images of Py in methanol- d_4 in 10 mm NMR tubes collected in the transverse and sagittal imaging planes (corresponding to two views of the 10 mm NMR tube filled with ~ 2 mL of HP Py solution and $1/16$ in. o.d. PTFE tubing) are shown in Figures 2 and 3,

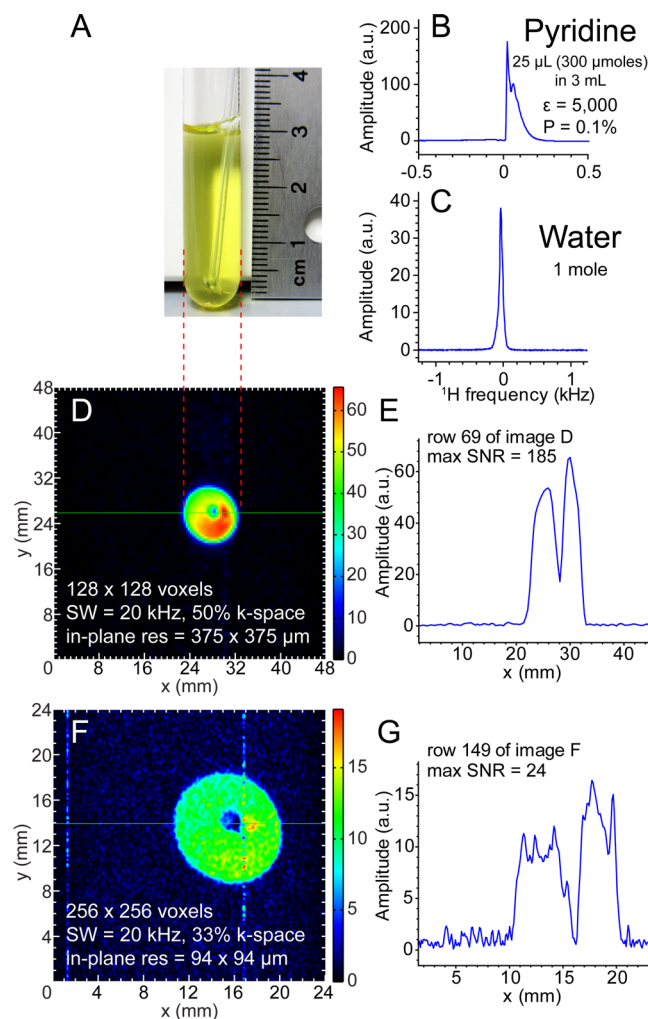


Figure 2. 47.5 mT proton NMR spectroscopy and transverse-plane proton imaging of SABRE-hyperpolarized Py. (A) A photograph of ~ 2 mL solution of 100 mM Py with 7 mM Ir catalyst in a 10 mm NMR tube with $1/16$ in. o.d. PTFE tubing for parahydrogen bubbling at 1 atm. (B,C) Single scan proton NMR spectra of HP Py (B) and that from a reference sample of water (~ 1 mol, part C). (D,E) Proton HP Py imaging with $375 \times 375 \mu\text{m}^2$ in-plane pixel resolution using GRE imaging and spatial NMR signal (“slice”) from the selected row. (F,G) Proton HP Py imaging with $94 \times 94 \mu\text{m}^2$ in-plane pixel resolution using GRE imaging and spatial NMR signal from the selected row. Total imaging times were ~ 3.9 s (D) and ~ 5.1 s (F), respectively. The imaging data was under-sampled using only a fraction of k-space encodings (50% and 33%, respectively).

respectively, at three different in-plane spatial resolutions. It should be noted that a 2D projection (i.e., without slice selection) gradient echo (GRE) sequence was used. This imaging sequence defined only pixel size (2D) with the most intense pixels lying in regions of greatest sample thickness but did not define the voxel size (3D). However, investigation of the resolution and sensitivity limits of potential *in vivo* HP low-field MRI motivated this study. Therefore, the voxel volume, V_{vox} of the most intense pixels used to ascertain these limits

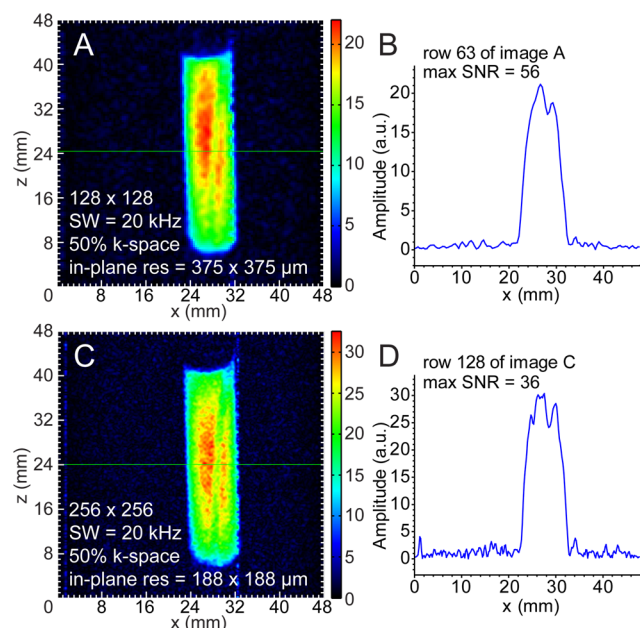


Figure 3. Sagittal-plane proton imaging of SABRE-polarized Py. (A,B) Proton HP Py with $375 \times 375 \mu\text{m}^2$ in-plane pixel resolution GRE imaging and spatial NMR signal (“slice”) from the selected row. (C,D) Proton HP Py $188 \times 188 \mu\text{m}^2$ in-plane pixel resolution GRE imaging and spatial NMR signal from the selected row. Total imaging times were ~ 3.9 s (A) and ~ 7.7 s (C), respectively.

was defined as the product of in-plane pixel resolution (as defined by the imaging sequence parameters) and the sample thickness at the location of the most intense pixel. This measure yielded the volumetric spatial resolution (in units of μm^3 or alternatively in mm^3), and in conjunction with the defined voxel’s associated measured signal-to-noise-ratio (SNR), SNR_{MAX} , was used for detection sensitivity analysis.

Four sets of ^1H images (Figures 2 and 3) were acquired from individual hyperpolarization preparations and yielded the following voxel sizes and SNRs for sensitivity analysis: $375 \times 375 \times 32\,000 \mu\text{m}^3$ ($V_{\text{vox}} = 4.5 \text{ mm}^3$, $\text{SNR}_{\text{MAX}} = 187$, Figure 2D), $94 \times 94 \times 32\,000 \mu\text{m}^3$ ($V_{\text{vox}} = 0.28 \text{ mm}^3$, $\text{SNR}_{\text{MAX}} = 24$, Figure 2F), $375 \times 375 \times 8750 \mu\text{m}^3$ ($V_{\text{vox}} = 1.2 \text{ mm}^3$, $\text{SNR}_{\text{MAX}} = 56$, Figure 3A), and $188 \times 188 \times 8750 \mu\text{m}^3$ ($V_{\text{vox}} = 0.31 \text{ mm}^3$, $\text{SNR}_{\text{MAX}} = 36$, Figure 3C). The $1/16$ in. PTFE tubing used for bubbling parahydrogen is clearly resolved in all four MR images. The 10 mm NMR tube was not placed perfectly coaxial with the imaging system’s z -axis, resulting in the observed tilt in the images.

Low-field HP ^{13}C images of $1\text{-}^{13}\text{C}$ -succinate- d_2 in water are shown in Figure 4. HP solutions were loaded into tilted 15 mL Falcon tubes and imaged in the coronal and sagittal planes (corresponding to two orientations of the Falcon tubes filled with ~ 1.5 mL of HP $1\text{-}^{13}\text{C}$ -succinate- d_2 solution and foam) with an in-plane spatial resolution of $250 \times 250 \mu\text{m}^2$. These two images were acquired from individual hyperpolarization preparations and corresponded to the following voxel sizes of $\sim 250 \times 250 \times 3000 \mu\text{m}^3$ ($V_{\text{vox}} = 0.19 \text{ mm}^3$, $\text{SNR}_{\text{MAX}} = 58$, Figure 4C) and $\sim 250 \times 250 \times 8000 \mu\text{m}^3$ ($V_{\text{vox}} = 0.50 \text{ mm}^3$, $\text{SNR}_{\text{MAX}} = 72$, Figure 4D). The brown arrows shown in Figure 4 indicate the presence of foamed contrast agent, a consequence of high-pressure ejection from the polarizer and HCA surface tension. Despite the magnetic susceptibility artifacts that typically accompany bubbles at high field, the

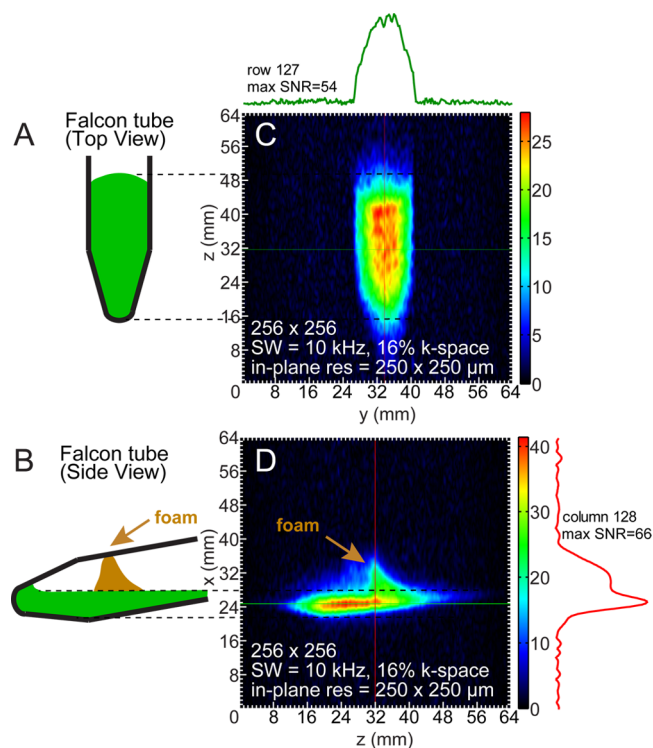


Figure 4. GRE imaging of ^{13}C PHIP-polarized $1\text{-}^{13}\text{C}$ -succinate- d_2 in a partially filled Falcon tube. (A,C) Coronal-plane cartoon and the corresponding image of ^{13}C -succinate $250 \times 250 \mu\text{m}^2$ in-plane pixel resolution GRE imaging with corresponding spatial NMR signal (“slice”) of the selected row. Total imaging time was ~ 4.5 s. (B,D) Sagittal-plane cartoon and the corresponding image of ^{13}C -succinate $250 \times 250 \mu\text{m}^2$ in-plane pixel resolution GRE imaging and spatial NMR signal from the selected column. Brown arrows mark the location of foamed HCA during in parts B and D.

foamed agent was amenable to imaging at the low field of 47.5 mT used here. The images in Figures 2F and 3C show differential-mode gradient amplifier noise, which a low-pass gradient filter would reduce or eliminate.

Under-sampling (i.e., data recording with 16–50% of the imaging matrix’s corresponding frequency-domain k -space points) did not cause any significant imaging artifacts (albeit some blurring is visible as in Figure 4) resulting from loss of information. The coherent k -space under-sampling scheme for each MRI acquisition was conducted using the built-in algorithm and routine of the Prosipa software environment (v3.12, Magritek, Wellington, New Zealand). Given the nonequilibrium nature of hyperpolarization, under-sampling k -space importantly decreases the total imaging acquisition time. For example, collecting only 50% of k -space projections accelerates acquisition by a factor of 2. The % of k -space sampled is therefore reported in Figures 2–4. Additional details about Prosipa’s under-sampling scheme can be found in the Supporting Information. Fast scan speeds are especially desirable for contrast agents with rapidly decaying polarization due to low T_1 , as exemplified by the agents used here. The MR images presented in Figures 2–4 and the Supporting Information were automatically reconstructed from the under-sampled data by Prosipa as supplied by the manufacturer. No additional data or image manipulations were performed to improve image quality, such as zero-filling or smoothing, beyond that as acquired and shown here and in the Supporting Information.

DISCUSSION

To the best of our knowledge (e.g., refs 24–30), the results shown here compare favorably with other low-field images of hyperpolarized or nonhyperpolarized media from the perspectives of both the achieved in-plane resolution as well as the small effective voxel sizes. Low-field, frequency-optimized rf coils comparable in SNR performance to commercial preclinical coils at 4.7 T for hyperpolarized contrast agents¹⁹ were used to achieve the high sensitivity necessary for microscale spatial resolution of ¹H and ¹³C HP MRI at low magnetic field. Figures 2–4 show that the required sensitivity is indeed attainable at a magnetic field strength of 47.5 mT. Not only the presented HP ¹H images but also the relatively large FOV ¹³C HP images are high-resolution owing to a large imaging matrix size (256 × 256 points) allowing small pixel sizes of only 250 × 250 μm² or less.

HyperBridge and HyperGate. These devices were essential for efficient preservation of nuclear spin hyperpolarization of 1-¹³C-succinate-*d*₂ (susceptible to depolarization in a near zero magnetic field) during transportation from the PHIP hyperpolarizer to the low-field MRI scanner. Overall, our experience is similar to others working with similar contrast agents.^{22,23} The range of magnetic field variation along the transfer path was almost entirely within the magnetic field bounds defined by the *T*₁ measurements at 5.75 mT and 47.5 mT. The HyperBridge and HyperGate may also prove useful for other similar HCAs such as 1-¹³C-phospholactate.³¹

Detection Sensitivity and Other Limits of Detection. The presented imaging results allow estimation of the corresponding detection sensitivity. Since HCA media can utilize variable % polarization and concentration or may involve detection of nuclei other than spin-1/2 nuclei (i.e., ¹H, ¹³C, ¹²⁹Xe, etc.), we were prompted to implement a new quantity of measure incorporating these variables as described below.

SNR in MRI^{19,32,33} is proportional to the gyromagnetic ratio, γ , concentration, *C*, and nuclear spin polarization, *P*, in a voxel volume, *V*_{VOX}, or

$$\text{SNR} = A\gamma CV_{\text{VOX}}P \quad (1)$$

where *A* is a numerical constant accounting for rf coil sensitivity, the imaging pulse sequence efficiency, and other experimental parameters. The value of this constant *A* yields a useful quantification of the detection sensitivity of the molecular imaging method because it can be used for direct comparison of imaging approaches and protocols. For example,

$$A_{\text{H}} = \text{SNR}_{\text{H}}/(\gamma_{\text{H}}C_{\text{H}}V_{\text{VOX}}P_{\text{H}}) \quad (2)$$

Here, we introduce the concept of fully (*P* = 1 = 100%) polarized proton spins (pps), wherein *A*_H γ _H in eq 2 is a useful quantity derived from the SNR from a hypothetical 1 mol of fully polarized proton spins (pps) in the imaging voxel of interest. When using the experimental results from Figure 3C (*C*_H = 0.5 M (5 Py protons at 0.1 M concentration) in 0.31 mm³ voxel volume with 0.1% polarization), *A*_H γ _H = 2.3 × 10¹¹ units of SNR per 1 mol of pps. The utility of this experimental rf-coil parameter lies in its enabling prediction of the SNR of biomedical imaging experiments with known metabolic fluxes, HCA concentrations, and anticipated % polarization on target hyperpolarized molecule.

For example, when using the low-field imaging setup (Figure 1) demonstrated in Figure 3C, if 1 mM concentration of proton spins with *P*_H = 0.01 (1%) is achieved in a tissue with an imaging voxel size of 10 mm³, one should expect a SNR of 23.

A SNR value >20 is sufficient for MRI image reconstruction as well as for quantitative *in vivo* imaging analysis of metabolite concentrations.³⁴ Moreover, this expected fine spatial resolution (i.e., voxel size of ~10 mm³) is similar to or better than that of high-field spectroscopic HP MRI performed with HCA with a significantly (factor of 10+) greater payload of net magnetization (i.e., *CV*_{VOX}*P*, eq 1)¹⁶ and represents nearly an order of magnitude improvement over the 50–100 mm³ voxel sizes of conventional high-field preclinical MR spectroscopy enabled by signal averaging of hundreds of scans.³⁵ A voxel size of ~10 mm³ already enables molecular imaging of deadly diseases such as cancer with isotropic spatial resolution of 2–3 mm, which can be further improved (to 1–2 mm range) through the use of more polarized media (e.g., *P* = 0.2 vs *P* = 0.01) or by exploiting metabolic pathways with higher metabolic fluxes and *in vivo* concentration (e.g., *C* = 10 mM vs 1 mM). Thus, the imaging sensitivity of HP low-field MRI certainly paves the way to molecular imaging of many metabolic pathways such as glycolysis^{13,16} or glutamine³⁶ and choline^{37,38} metabolism, which are often up-regulated in cancer and other diseases, with spatial resolution (defined as the pixel size) exceeding that of micro-PET (>2 mm in each dimension).³⁹

It should also be stressed that the effective spectroscopic line-width corresponding to *B*₀ field homogeneity is typically limited only by the homogeneity of the magnet at low magnetic fields (our study) rather than by subject-induced perturbations to *B*₀ (i.e., inhomogeneity due to tissue magnetic susceptibility) at high magnetic fields. In addition, subject-associated rf (also referred to as *B*₁) losses are negligible at low resonance frequencies.²⁰ Therefore, the SNR factor analysis performed above is fully applicable to *in vivo* conditions.

A corresponding analysis applies to ¹³C imaging. When using the experimental parameters in Figure 4C (*C* = 0.030 M, %*P* = 14.2%, *V*_{VOX} = 0.19 mm³, SNR = 54), *A*_{13C} γ _{13C} = 6.7 × 10¹⁰ units of SNR per 1 mol of ¹³C polarized spins (cps, i.e., 100% polarized ¹³C nuclei). It should be noted that $\gamma_{13\text{C}} = \gamma_{\text{H}}/3.98$, and consequently it is unsurprising that *A*_{13C} γ _{13C} in units of cps is significantly lower than *A*_H γ _H. It reflects the inherently greater NMR sensitivity of protons with their greater magnetic moment under otherwise identical conditions compared to those of ¹³C spins. However, *A*_{13C} γ _{13C} of the ¹³C rf coil can be expressed in units of pps (corresponding to HP proton imaging in the ¹³C rf coil at 3.98 times lower *B*₀) yielding *A*_{13C} γ _H = 2.7 × 10¹¹ units of SNR per 1 mol of pps. This value of *A*_{13C} γ _H is very similar to *A*_H γ _H despite an ~4-fold difference in the resonance frequency (0.508 MHz vs 2.02 MHz). This agreement is consistent with our recent work demonstrating a very weak MR SNR dependence on the resonance frequency (SNR ∝ $\omega_0^{0.25}$) for this type of MRI rf coil.¹⁹ Moreover, this result indicates that high-resolution and high-sensitivity (i.e., large *A* γ values) MRI of HCA should be readily achieved at even lower magnetic fields. Although future hardware and imaging-sequence improvements can certainly improve *A* γ , low-field MRI still largely remains unexplored territory, the values already reported here demonstrate the feasibility of *in vivo* preclinical imaging using HCAs.

Feasibility of Direct Proton HCA Imaging *in Vivo*.

While protons are the most sensitive MRI nuclei, the direct proton imaging of HP MRI contrast media is challenging at high magnetic fields because of background signal from ~10² M protons.⁴⁰ A potential mitigation is indirect proton imaging of ¹³C HCA by initial water suppression, followed by intra-molecular polarization transfer from HP ¹³C to ¹H, with final

imaging of proton spins.^{41,42} While this approach has been demonstrated at high field, it poses two challenges: (i) efficient water background suppression and (ii) the requirement of ¹³C isotopic labeling. Fundamentally, for direct proton HCA imaging, the condition $C_{\text{HCA}} \times P_{\text{HCA}} \gg C_{\text{B}} \times P_{\text{B}}$ (or $C_{\text{HCA}} \gg C_{\text{B}} \times P_{\text{B}}/P_{\text{HCA}}$) must be met (where C_{HCA} , C_{B} , P_{HCA} , and P_{B} correspond to the concentrations and polarizations of HCA and the background proton species, respectively). The low B_0 magnetic field used here reduces proton background by orders of magnitude, reduction of B_0 linearly decreases P_{B} . Reasonably assuming that $\%P_{\text{HCA}} = 10\%$, corresponding to an enhancement factor of 6×10^5 (i.e., $P_{\text{HCA}}/P_{\text{B}}$) at 47.5 mT and water proton concentration of $\sim 10^2$ M, C_{HCA} during image acquisition must be significantly greater than 0.2 mM, which makes direct proton imaging of many HP metabolites above the 1 mM level feasible. Moreover, further minimization of the ratio $C_{\text{B}} \times P_{\text{B}}/P_{\text{HCA}}$ simply entails additional reduction of B_0 .

Low-Field MRI Hardware Challenges and Opportunities. A key metric of MRI rf coil performance is the quality factor Q ($\omega_0/\Delta\omega_0$) of the rf receiver network, where $\Delta\omega_0$ corresponds to the -3 dB bandwidth of the matched rf circuit resonance at the detection frequency ω_0 . The use of high-sensitivity coils implies a high Q , which limits the maximum spectroscopic imaging bandwidth (SW). High SW is required for high-resolution MRI with large imaging matrices, because $\Delta\omega_0$ must be greater than SW to avoid imaging artifacts.⁴³ The rf circuits used here had Q values of 62 at 2.02 MHz and 28 at 0.508 MHz corresponding to $\Delta\omega_0$ of 32 kHz and 18 kHz, respectively. Therefore, nearly the maximum SWs of 20 kHz and 10 kHz were utilized. However, use of high- Q yet low-SW rf coils would advantageously enable greater values of the SNR and $A\gamma$ constant. A potential solution to these contradictory requirements (high- Q coils versus high-SW MRI) without loss of SNR as noted by Baudin et al.⁴³ involves rf probe Q -spoiling by active feedback to increase the imaging bandwidth at low resonance frequencies. Such Q -spoiling is most desirable as it simultaneously enables MRI using high- Q rf probes for high-SW imaging at very low resonance frequencies.

CONCLUSION

High-resolution ($94 \times 94 \mu\text{m}^2$) MRI of proton and ¹³C HP contrast agents has been demonstrated at a low magnetic field of 47.5 mT. The achieved spatial resolution of the presented molecular imaging rivals that of micro-PET.³⁹ The HyperBridge and HyperGate magnetic devices were successfully demonstrated for transportation of hyperpolarized contrast agents from the hyperpolarizer to the preclinical low-field MRI scanner. The presented technological advances of low-field MRI already can enable preclinical molecular imaging of proton and ¹³C hyperpolarized contrast agents, and there are no fundamental barriers for future clinical translation. For example, DNP hyperpolarized 1-¹³C-pyruvate is already being used in clinical trials.⁵ With respect to parahydrogen-based methods for hyperpolarization, hyperpolarized succinates and hyperpolarized phospholactate are particularly well-suited for molecular imaging using the technologies described here. ¹³C-succinates potentially report on abnormal citric acid cycle metabolism in cancer.^{4,44,45} 1-¹³C-phospholactate can be hyperpolarized via PHIP to $\%P_{13\text{C}} > 15\%$.⁴⁶ When injected into living organisms, 1-¹³C-phospholactate is rapidly dephosphorylated (within seconds) to 1-¹³C-lactate⁴⁷ and therefore can be potentially used for cancer imaging in similar fashion to DNP hyperpolarized 1-¹³C-lactate and 1-¹³C-pyruvate.^{48,49} However, one

advantage for hyperpolarized ¹³C-lactate compared to ¹³C-pyruvate is the fact that it can be used within a physiologically relevant *in vivo* concentration range.⁴⁸

Other technical improvements in low-field rf coil development involve the use of superconducting or cryogenically cooled rf coils to increase the detection sensitivity by several fold,^{50,51} leading to concomitant improvements in the resolution limits. Furthermore, the use of compressed sensing in conjunction with faster and more sensitive imaging sequences³⁰ can further improve the detection sensitivity and accelerate total imaging time.

METHODS

PHIP/SABRE Polarizer. A 5.75 mT electromagnet-based polarizer produced the SABRE-polarized pyridine and PHIP-polarized 1-¹³C-succinate- d_2 . Details of the polarizer are summarized in Supporting Information text. Briefly, the polarizer is fully automated with a console-based graphical user interface. The polarizer controller unit employs open-source computer software applied in previous work^{8,52,53} and utilizes a chemical reactor, mixing manifold, and rf probe design similar to ones reported earlier.^{21,54}

47.5 mT MRI System. Low-field MR spectra and images were acquired using a 47.5 mT MR scanner (89 mm i.d. bore) equipped with Prospa software (version 3.12, Magritek, Wellington, New Zealand). Previously developed, 38 mm i.d. dual-channel rf probes were used for imaging in ¹³C/¹H and ¹H/¹³C configurations. These probes have crystal-radio solenoid rf coils whose detection sensitivity was optimized for the primary (first-listed) channel's resonance frequency ω_0 (2.02 MHz for ¹H, X tuned to 0.508 MHz for ¹³C).¹⁹

Production and Transfer of HP Contrast Media. An N-heterocyclic carbene complex-based Ir catalyst^{55,56} was prepared as described previously.^{57,58} Solutions (~ 2 mL) of the Ir-catalyst and Py substrate in methanol- d_4 were used for SABRE hyperpolarization in a standard 10 mm NMR tube with ~ 7 mM [IrCl(COD)(IMes)]⁵⁷ [IMes = 1,3-bis(2,4,6-trimethylphenyl), imidazole-2-ylidene; COD = cyclooctadiene] catalyst concentration and ~ 100 mM Py substrate concentration. For SABRE, the polarizer was operated with the rf probe removed with an estimated solution temperature of ~ 40 °C. Ultrahigh purity ($>99.999\%$ H₂) parahydrogen gas with $>90\%$ para-state⁵⁹ was bubbled through the solution for 2 min to generate HP pyridine.^{56,60} Immediately after cessation of bubbling, the HP Py was transferred through Earth's field to the imaging system (see the Supporting Information for details), where images were obtained ~ 12 s after hyperpolarization, a time sufficient to significantly depolarize HP Ir-hydride and HP ortho-H₂ ($T_1 \sim 2$ – 3 s at 9.4 T in these solutions) but not HP Py ($T_1 \sim 21$ s at 9.4 T⁵⁸ and $T_1 = 11.1 \pm 0.1$ s at 47.5 mT). ¹³C HP 1-¹³C-succinate- d_2 ⁶¹ was produced using the PASADENA⁶² method, employing 30 mM 1-¹³C-fumaric acid- d_2 precursor in aqueous medium at pH > 9 and 5 mM Rh(I) catalyst. The Rh(I) catalyst was prepared as described previously⁶³ using bis(norbornadiene)rhodium(I) tetrafluoroborate (Strem no. 45-0230, Newburyport, MA) and 1,4-bis[(phenyl-3-propanesulfonate) phosphine]butane (no. 717347, Sigma-Aldrich-Isotec, OH). The $\%$ polarization of the HP 1-¹³C-succinate- d_2 was tested *in situ*²¹ of the PHIP polarizer. All handling of the HP 1-¹³C-succinate- d_2 prior to sample insertion into the low-field imaging system took place in magnetic fields generated by the "HyperBridge" and "HyperGate" to preserve hyperpolarization (Supporting Information

text), Figure 1. Images were obtained from $\sim 45 \mu\text{mol}$ of HCA in 1.5 mL of water loaded into a 15 mL Falcon tube (part 14-959-70C, Fisher Scientific). Because only one low-field MR console was available for PHIP $^1\text{H} \rightarrow ^{13}\text{C}$ hyperpolarization transfer and low-field MRI, the rf cables had to be switched (from PHIP probe to MRI probe) after $1\text{-}^{13}\text{C}$ -succinate- d_2 PHIP in order to acquire images. Further details are given in the Supporting Information text.

Imaging Protocol/Parameters. One 2D gradient echo (GRE) image without slice selection was acquired from each freshly polarized individual HCA batch using a planar GRE imaging sequence provided in Prospa software, where the parameters varied for MRI acquisition in two mutually orthogonal imaging planes. Proton Py images used 128×128 or 256×256 pixel matrices over fields of view (FOV) ranging from $24 \times 24 \text{ mm}^2$ to $64 \times 64 \text{ mm}^2$ with corresponding k -space under-sampling (defined as percentage of acquired k -space projections). Py GRE imaging parameters for $375 \times 375 \mu\text{m}^2$ in-plane pixel resolution were echo time (TE) = 7 ms, repetition time (TR) = 60 ms (limited by the electronics response time), and time of acquisition (t_{Acq}) = 6.4 ms. Imaging parameters for $188 \times 188 \mu\text{m}^2$ and $94 \times 94 \mu\text{m}^2$ in-plane pixel resolution images were TE = 13 ms, TR = 60 ms, and t_{Acq} = 12.8 ms. Other imaging parameters are provided in Figures 2 and 3. Quality assurance reporting on the level of $\%P_{\text{H}}$ of the HCA before imaging at 47.5 mT was performed with 90° square excitation rf pulses in a separate experimental series. For the ^{13}C HCA, $\%P_{^{13}\text{C}}$ was measured spectroscopically in the MRI scanner immediately after the sample transfer from PHIP polarizer via the HyperBridge and HyperGate (using a 15° square rf excitation pulse). GRE imaging followed immediately after spectroscopic polarization measurements. All ^{13}C imaging of $1\text{-}^{13}\text{C}$ -succinate- d_2 was performed with a $64 \times 64 \text{ mm}^2$ FOV, TE = 26 ms, TR = 110 ms (limited by the electronics response time), t_{Acq} = 25.6 ms, and a fixed pulse angle of 30° . Other imaging parameters are provided in Figure 4.

■ ASSOCIATED CONTENT

■ Supporting Information

Additional details regarding PHIP hyperpolarizer, low-field MRI system, hyperpolarized contrast agent production and transfer, and MRI imaging. This material is available free of charge via the Internet at <http://pubs.acs.org>.

■ AUTHOR INFORMATION

Corresponding Author

*E-mail: eduard.chekmenev@vanderbilt.edu.

Notes

The authors declare no competing financial interest.

■ ACKNOWLEDGMENTS

This work was supported by the RAS (5.1.1), RFBR (Grants 14-03-00374-a, 14-03-31239-mol-a, 12-03-00403-a), SB RAS (Grants 57, 60, 61, 122), the Ministry of Education and Science of the Russian Federation, and the Council on Grants of the President of the Russian Federation (Grant MK-4391.2013.3). We thank for funding support NIH Grants ICMIC 5P50 CA128323-03, 5R00 CA134749-03, 3R00CA134749-02S1, and DoD CDMRP Breast Cancer Program Era of Hope Award W81XWH-12-1-0159/BC112431.

■ REFERENCES

- (1) Weissleder, R. *Science* **2006**, *312*, 1168–1171.
- (2) Gambhir, S. S. *Nat. Rev. Cancer* **2002**, *2*, 683–693.
- (3) Kobayashi, H.; Choyke, P. L. *Acc. Chem. Res.* **2010**, *44*, 83–90.
- (4) Kurhanewicz, J.; Vigneron, D. B.; Brindle, K.; Chekmenev, E. Y.; Comment, A.; Cunningham, C. H.; DeBerardinis, R. J.; Green, G. G.; Leach, M. O.; Rajan, S. S.; Rizi, R. R.; Ross, B. D.; Warren, W. S.; Malloy, C. R. *Neoplasia* **2011**, *13*, 81–97.
- (5) Nelson, S. J.; Kurhanewicz, J.; Vigneron, D. B.; Larson, P. E. Z.; Harzstark, A. L.; Ferrone, M.; van Crielinge, M.; Chang, J. W.; Bok, R.; Park, I.; Reed, G.; Carvajal, L.; Small, E. J.; Munster, P.; Weinberg, V. K.; Ardenkjaer-Larsen, J. H.; Chen, A. P.; Hurd, R. E.; Odegardstuen, L. I.; Robb, F. J.; Tropp, J.; Murray, J. A. *Sci. Transl. Med.* **2013**, *5*, No. 198ra108.
- (6) Abragam, A.; Goldman, M. *Rep. Prog. Phys.* **1978**, *41*, 395–467.
- (7) Ardenkjaer-Larsen, J. H.; Fridlund, B.; Gram, A.; Hansson, G.; Hansson, L.; Lerche, M. H.; Servin, R.; Thaning, M.; Golman, K. *Proc. Natl. Acad. Sci. U.S.A.* **2003**, *100*, 10158–10163.
- (8) Nikolaou, P.; Coffey, A. M.; Walkup, L. L.; Gust, B. M.; Whiting, N.; Newton, H.; Barcus, S.; Muradyan, L.; Dabaghyan, M.; Moroz, G. D.; Rosen, M.; Patz, S.; Barlow, M. J.; Chekmenev, E. Y.; Goodson, B. M. *Proc. Natl. Acad. Sci. U.S.A.* **2013**, *110*, 14150–14155.
- (9) Jannin, S.; Bornet, A.; Melzi, R.; Bodenhausen, G. *Chem. Phys. Lett.* **2012**, *549*, 99–102.
- (10) Eischenschmidt, T. C.; Kirss, R. U.; Deutsch, P. P.; Hommeltoft, S. I.; Eisenberg, R.; Bargon, J.; Lawler, R. G.; Balch, A. L. *J. Am. Chem. Soc.* **1987**, *109*, 8089–8091.
- (11) Adams, R. W.; Aguilar, J. A.; Atkinson, K. D.; Cowley, M. J.; Elliott, P. I. P.; Duckett, S. B.; Green, G. G. R.; Khazal, I. G.; Lopez-Serrano, J.; Williamson, D. C. *Science* **2009**, *323*, 1708–1711.
- (12) Bowers, C. R.; Weitekamp, D. P. *Phys. Rev. Lett.* **1986**, *57*, 2645–2648.
- (13) Golman, K.; in't Zandt, R.; Thaning, M. *Proc. Natl. Acad. Sci. U.S.A.* **2006**, *103*, 11270–11275.
- (14) Golman, K.; Petersson, J. S. *Acad. Radiol.* **2006**, *13*, 932–942.
- (15) Brindle, K. M.; Bohndiek, S. E.; Gallagher, F. A.; Kettunen, M. I. *Magn. Reson. Med.* **2011**, *66*, S05–S19.
- (16) Day, S. E.; Kettunen, M. I.; Gallagher, F. A.; Hu, D. E.; Lerche, M.; Wolber, J.; Golman, K.; Ardenkjaer-Larsen, J. H.; Brindle, K. M. *Nat. Med.* **2007**, *13*, 1382–1387.
- (17) Albers, M. J.; Bok, R.; Chen, A. P.; Cunningham, C. H.; Zierhut, M. L.; Zhang, V. Y.; Kohler, S. J.; Tropp, J.; Hurd, R. E.; Yen, Y.-F.; Nelson, S. J.; Vigneron, D. B.; Kurhanewicz, J. *Cancer Res.* **2008**, *68*, 8607–8615.
- (18) Ardenkjaer-Larsen, J. H.; Leach, A. M.; Clarke, N.; Urbahn, J.; Anderson, D.; Skloss, T. W. *NMR Biomed.* **2011**, *24*, 927–932.
- (19) Coffey, A. M.; Truong, M. L.; Chekmenev, E. Y. *J. Magn. Reson.* **2013**, *237*, 169–174.
- (20) Hayden, M. E.; Bidinosti, C. P.; Chapple, E. M. *Concepts Magn. Reson., Part A* **2012**, *40A*, 281–294.
- (21) Waddell, K. W.; Coffey, A. M.; Chekmenev, E. Y. *J. Am. Chem. Soc.* **2011**, *133*, 97–101.
- (22) Bornet, A.; Melzi, R.; Linde, A. J. P.; Hautle, P.; van den Brandt, B.; Jannin, S.; Bodenhausen, G. *J. Phys. Chem. Lett.* **2013**, *4*, 111–114.
- (23) Cheng, T.; Mishkovsky, M.; Bastiaansen, J. A.; Ouari, O.; Hautle, P.; Tordo, P.; van den Brandt, B.; Comment, A. *NMR Biomed.* **2013**, *26*, 1582–1588.
- (24) Venkatesh, A. K.; Zhang, A. X.; Mansour, J.; Kubatina, L.; Oh, C. H.; Blasche, G.; Unlu, M. S.; Balamore, D.; Jolesz, F. A.; Goldberg, B. B.; Albert, M. S. *Magn. Reson. Imaging* **2003**, *21*, 773–776.
- (25) Matter, N. I.; Scott, G. C.; Venook, R. D.; Ungersma, S. E.; Grafendorfer, T.; Macovski, A.; Conolly, S. M. *Magn. Reson. Med.* **2006**, *56*, 1085–1095.
- (26) Ruset, I. C.; Tsai, L. L.; Mair, R. W.; Patz, S.; Hrovat, M. I.; Rosen, M. S.; Muradian, I.; Ng, J.; Topulos, G. P.; Butler, J. P.; Walsworth, R. L.; Hersman, F. W. *Concepts Magn. Reson., Part B* **2006**, *29B*, 210–221.
- (27) Krjukov, E.; Fichelle, S.; Wild, J. M.; Paley, M. N. J. *Concepts Magn. Reson., Part B* **2007**, *31B*, 209–217.

- (28) Tsai, L. L.; Mair, R. W.; Rosen, M. S.; Patz, S.; Walsworth, R. L. *J. Magn. Reson.* **2008**, *193*, 274–285.
- (29) Scheenen, T. W. J.; Futterer, J.; Weiland, E.; van Hecke, P.; Lemort, M.; Zechmann, C.; Schlemmer, H. P.; Broome, D.; Villeirs, G.; Lu, J. P.; Barentsz, J.; Roell, S.; Heerschap, A. *Invest. Radiol.* **2011**, *46*, 25–33.
- (30) Sarraçanie, M.; Armstrong, B. D.; Stockmann, J.; Rosen, M. S. *Magn. Reson. Med.* **2014**, *71*, 735–745.
- (31) Shchepin, R. V.; Coffey, A. M.; Waddell, K. W.; Chekmenev, E. Y. *J. Am. Chem. Soc.* **2012**, *134*, 3957–3960.
- (32) Hoult, D. I.; Richards, R. E. *J. Magn. Reson.* **1976**, *213*, 329–343.
- (33) Hoult, D. I.; Lauterbur, P. C. *J. Magn. Reson.* **1979**, *34*, 425–433.
- (34) Sharma, U.; Baek, H. M.; Su, M. Y.; Jagannathan, N. R. *NMR Biomed.* **2011**, *24*, 700–711.
- (35) Pfeuffer, J.; Tkac, I.; Provencher, S. W.; Gruetter, R. J. *Magn. Reson.* **1999**, *141*, 104–120.
- (36) Gallagher, F. A.; Kettunen, M. I.; Day, S. E.; Lerche, M.; Brindle, K. M. *Magn. Reson. Med.* **2008**, *60*, 253–257.
- (37) Dorrius, M. D.; Pijnappel, R. M.; Jansen-van der Weide, M. C.; Jansen, L.; Kappert, P.; Oudkerk, M.; Sijens, P. E. *Radiology* **2011**, *259*, 695–703.
- (38) Keshari, K. R.; Tsachres, H.; Iman, R.; Delos Santos, L.; Tabatabai, Z. L.; Shinohara, K.; Vigneron, D. B.; Kurhanewicz, J. *NMR Biomed.* **2011**, *24*, 691–699.
- (39) Popota, F. D.; Aguiar, P.; Herance, J. R.; Pareto, D.; Rojas, S.; Ros, D.; Pavia, J.; Gispert, J. D. *IEEE Trans. Nucl. Sci.* **2012**, *59*, 1879–1886.
- (40) Hövener, J.-B.; Schwaderlapp, N.; Borowiak, R.; Lickert, T.; Duckett, S. B.; Mewis, R. E.; Adams, R. W.; Burns, M. J.; Highton, L. A. R.; Green, G. G. R.; Olaru, A.; Hennig, J.; von Elverfeldt, D. *Anal. Chem.* **2014**, *86*, 1767–1774.
- (41) Mishkovsky, M.; Cheng, T.; Comment, A.; Gruetter, R. *Magn. Reson. Med.* **2012**, *68*, 349–352.
- (42) Truong, M. L.; Coffey, A. M.; Shchepin, R. V.; Waddell, K. W.; Chekmenev, E. Y. *Contrast Media Mol. Imaging* **2014**, DOI: 10.1002/cmmi.1579.
- (43) Baudin, E.; Safiullin, K.; Morgan, S. W.; Nacher, P. J. *J. Phys.: Conf. Ser.* **2011**, *294*, 012009.
- (44) Bhattacharya, P.; Chekmenev, E. Y.; Perman, W. H.; Harris, K. C.; Lin, A. P.; Norton, V. A.; Tan, C. T.; Ross, B. D.; Weitekamp, D. P. *J. Magn. Reson.* **2007**, *186*, 150–155.
- (45) Zacharias, N. M.; Chan, H. R.; Sailasuta, N.; Ross, B. D.; Bhattacharya, P. *J. Am. Chem. Soc.* **2012**, *134*, 934–943.
- (46) Shchepin, R. V.; Coffey, A. M.; Waddell, K. W.; Chekmenev, E. Y. *Anal. Chem.* **2014**, *86*, 5601–5605.
- (47) Shchepin, R. V.; Pham, W.; Chekmenev, E. Y. *J. Labelled Compd. Radiopharm.* **2014**, *57*, 517–524.
- (48) Kennedy, B. W. C.; Kettunen, M. I.; Hu, D.-E.; Brindle, K. M. *J. Am. Chem. Soc.* **2012**, *134*, 4969–4977.
- (49) Kettunen, M. I.; Kennedy, B. W. C.; Hu, D.-e.; Brindle, K. M. *Magn. Reson. Med.* **2012**, *70*, 1200–1209.
- (50) Darrasse, L.; Ginefri, J. C. *Biochimie* **2003**, *85*, 915–937.
- (51) Resmer, F.; Seton, H. C.; Hutchison, J. M. S. *J. Magn. Reson.* **2010**, *203*, 57–65.
- (52) Nikolaou, P.; Coffey, A. M.; Walkup, L. L.; Gust, B.; LaPierre, C.; Koehnemann, E.; Barlow, M. J.; Rosen, M. S.; Goodson, B. M.; Chekmenev, E. Y. *J. Am. Chem. Soc.* **2014**, *136*, 1636–1642.
- (53) Nikolaou, P.; Coffey, A. M.; Walkup, L. L.; Gust, B. M.; Whiting, N. R.; Newton, H.; Muradyan, I.; Dabaghyan, M.; Ranta, K.; Moroz, G.; Patz, S.; Rosen, M. S.; Barlow, M. J.; Chekmenev, E. Y.; Goodson, B. M. *Magn. Reson. Imaging* **2014**, *32*, 541–550.
- (54) Coffey, A. M.; Shchepin, R. V.; Wilkens, K.; Waddell, K. W.; Chekmenev, E. Y. *J. Magn. Reson.* **2012**, *220*, 94–101.
- (55) Cowley, M. J.; Adams, R. W.; Atkinson, K. D.; Cockett, M. C. R.; Duckett, S. B.; Green, G. G. R.; Lohman, J. A. B.; Kerssebaum, R.; Kilgour, D.; Mewis, R. E. *J. Am. Chem. Soc.* **2011**, *133*, 6134–6137.
- (56) Zeng, H.; Xu, J.; Gillen, J.; McMahon, M. T.; Artemov, D.; Tyburn, J. M.; Lohman, J. A.; Mewis, R. E.; Atkinson, K. D.; Green, G. G.; Duckett, S. B.; van Zijl, P. C. *J. Magn. Reson.* **2013**, *237C*, 73–78.
- (57) Vazquez-Serrano, L. D.; Owens, B. T.; Buriak, J. M. *Inorg. Chim. Acta* **2006**, *359*, 2786–2797.
- (58) Barskiy, D. A.; Kovtunov, K. V.; Koptug, I. V.; He, P.; Groome, K. A.; Best, Q. A.; Shi, F.; Goodson, B. M.; Shchepin, R. V.; Coffey, A. M.; Waddell, K. W.; Chekmenev, E. Y. *J. Am. Chem. Soc.* **2014**, *136*, 3322–3325.
- (59) Feng, B. B.; Coffey, A. M.; Colon, R. D.; Chekmenev, E. Y.; Waddell, K. W. *J. Magn. Reson.* **2012**, *214*, 258–262.
- (60) Borowiak, R.; Schwaderlapp, N.; Huethe, F.; Lickert, T.; Fischer, E.; Bar, S.; Hennig, J.; von Elverfeldt, D.; Hövener, J. B. *Magn. Reson. Mater. Phys.* **2013**, *26*, 491–499.
- (61) Chekmenev, E. Y.; Hövener, J.; Norton, V. A.; Harris, K.; Batchelder, L. S.; Bhattacharya, P.; Ross, B. D.; Weitekamp, D. P. *J. Am. Chem. Soc.* **2008**, *130*, 4212–4213.
- (62) Bowers, C. R.; Weitekamp, D. P. *J. Am. Chem. Soc.* **1987**, *109*, 5541–5542.
- (63) Cai, C.; Coffey, A. M.; Shchepin, R. V.; Chekmenev, E. Y.; Waddell, K. W. *J. Phys. Chem. B* **2013**, *117*, 1219–1224.